SPECKLE FILTERING AND PHYSICAL SCATTERING DECOMPOSITION FOR ALOS-2 PALSAR-2 POLARIMETRIC MOSAIC

Ken Yoong LEE, Chen Guang HOU, Soo Chin LIEW, Leong Keong KWOH

Centre for Remote Imaging, Sensing and Processing
National University of Singapore
18 Kent Ridge Road, Singapore 119227
Email: {crslky, crshc, scliew, crsklk}@nus.edu.sg

KEY WORDS: ALOS-2 PALSAR-2, geocoding, mosaicking, speckle filtering, physical scattering decomposition

ABSTRACT: This paper presents the speckle filtering and physical scattering decomposition for the ALOS-2 PALSAR-2 fully polarimetric mosaic. The processing steps include 1) multi-looking, 2) speckle filtering, 3) geocoding, 4) mosaicking, and 5) model-based polarimetric decomposition. Another variant of iterative bilateral filter, called gravitational filter, was assessed for polarimetric speckle filtering. Benchmarking against the refined Lee filter and the boxcar filter, the experimental results on the ALOS-2 PALSAR-2 polarimetric data confirmed the effectiveness of the gravitational filter in speckle reduction and image feature retention. Prior to the mosaicking, the geodetic coordinates of selected control points, which were given based on the Geodetic Reference System 1980, were first converted into the Universal Transverse Mercator map coordinates. Subsequently, the ALOS-2 PALSAR-2 speckle-filtered data were geocoded by using second-order polynomial equation and least squares method. For the polarimetric scattering decomposition, an iterative multistage four-component decomposition was applied to the ALOS-2 PALSAR-2 polarimetric mosaic. From the decomposition result, a large amount of negative power pixels over vegetated areas were reduced. The total number of the remaining negative power pixels was only 0.006%.

1. INTRODUCTION

Since the launch of Seasat in year 1978, spaceborne synthetic aperture radar (SAR) has been an integral part of remote sensing for earth observation. Being an active imaging system, SAR can operate both day and night under all weather conditions. Moreover, it can also provide a vast number of cloud-free remotely sensed data. To date, there exist many published works dealing with geocoding and mosaicking of spaceborne SAR imagery. Among the relevant papers are Curlander (1984), Curlander *et al.* (1987), Kwok *et al.* (1990), Schreier *et al.* (1990), Kwoh *et al.* (1997), Shimada and Isoguchi (2002), Shimada and Ohtaki (2010), Antropov *et al.* (2012), Syrris *et al.* (2020), etc. The generated regional- and global-scale SAR mosaics present very meaningful synoptic views of the Earth's landmass.

With the realisation of fully polarimetric SAR (PolSAR) imaging systems, polarisation diversity has received a tremendous boost and becomes common in spaceborne SAR, for instances, ALOS-1, ALOS-2, RADARSAT-2, SAOCOM, COSMO-SkyMed, etc. The acquired fully PolSAR data offer interesting and valuable opportunities in understanding and quantifying physical interaction behaviours between radar waves and the illuminated Earth's surface through the available scattering matrix or polarimetric covariance matrix (Cloude, 2009; Lee and Pottier, 2009; van Zyl and Kim, 2011; Yamaguchi, 2020). However, speckle appears inherently in the PolSAR data due to random interference of coherent echoes from many elementary scatterers within an illuminated resolution cell. The presence of speckle noise can degrade the reliability of the extracted physical scattering properties and complicate the interpretation of the fully PolSAR data.

This paper examines a recently proposed polarimetric speckle filter, called gravitational filter, for an improved retrieval of physical scattering mechanisms from the ALOS-2 PALSAR-2 fully polarimetric mosaic. The ALOS-2 PALSAR-2 test data were described in Section 2. Section 3 presents the methodology of this research study. The obtained speckle filtering and polarimetric scattering decomposition results are discussed in Section 4. Finally, conclusions are drawn in Section 5.

2. DATA ACQUISITION

Covering the whole area of Singapore, two ALOS-2 PALSAR-2 high-sensitive quad-polarisation data (level 1.1), which were provided by the Japan Aerospace Exploration Agency (JAXA), were employed in this study. Table 1 lists the details of the two single-look complex (SLC) test data, which were collected on the descending orbit. Each test dataset contains four image files, one leader file, one volume directory file, and one trailer file. The corresponding product format description can be found at https://www.eorc.jaxa.jp/ALOS-2/en/doc/format.htm.

Table 1: Specifications of ALOS-2 PALSAR-2 test data

Scene identifier	ALOS2105433590-160506	ALOS2107503590-160520
Observation date	6ᵗʰ May 2016	20ᵗʰ May 2016
Scene centre time	04:50:36.372 UTC	04:50:36.517 UTC
Beam number	FP6-6	FP6-5
Radar wavelength	24.24525 cm	
Software identifier	2.025	2.028
Incidence angle at scene center	36.501°	33.861°
Line spacing (m)	2.7996337	3.2152384
Pixel spacing (m)	2.8608445	2.8608445

3. METHODOLOGY

As shown in Figure 1, the processing tasks comprise 1) multi-looking, 2) speckle filtering, 3) geocoding, 4) mosaicking, and 5) physical scattering decomposition. Each processing step is explained further in the following subsections.
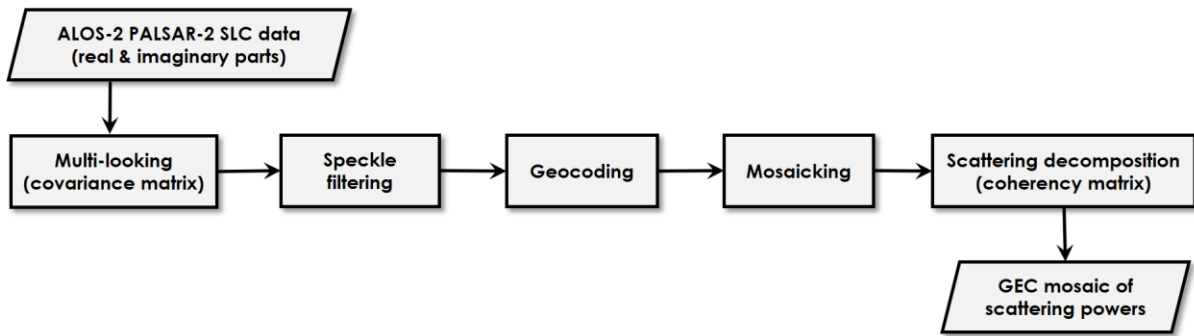

Figure 1: Outline of methodology, where GEC means geocoded ellipsoid corrected.

3.1 Multi-looking

After symmetrising the cross-polarised responses, the complex vector of each pixel in the ALOS-2 PALSAR-2 single-look slant-range data is given by

$$\mathbf{s} = c \begin{bmatrix} I_{HH} + jQ_{HH} \\ \{(I_{HV} + I_{VH}) + j(Q_{HV} + Q_{VH})\}/\sqrt{2} \\ I_{VV} + jQ_{VV} \end{bmatrix}, \qquad (1)$$

where $j = \sqrt{-1}$. The 32-bit in-phase and quadrature components are represented separately by I and Q. The scalar c in (1) equals to $10^{(CF - 32)/20}$, where CF is the calibration factor. As retrieved from the radiometric data record in the leader file, the CF takes a value of −83. A four-look $q \times q$ ($q = 3$) polarimetric covariance matrix was formed in this study by taking 2×2 neighbouring pixels:

$$\mathbf{C} = \frac{1}{L} \sum_{i=1}^{L} \mathbf{s}_i \mathbf{s}_i^{*T}, \qquad (2)$$

where L refers to the number of looks (i.e., $L = 4$). The superscripts $*$ and T denote the complex conjugate and transpose, respectively.

3.2 Speckle Filtering

As named by Tomasi and Manduchi (1998), bilateral filter is a locally adaptive weighted averaging filter, which can be applied in an iterative way. Its filtering weight takes spatial closeness and radiometric similarity into account. Often the filtering weight is derived from an exponential family, e.g., normal distribution. Such a bilateral filter is also known as nonlinear edge preserving Gaussian filter, which was proposed by Aurich and Weule (1995). The extensions and applications of the bilateral filter for polarimetric speckle filtering can be found in Alonso-González *et al.* (2013), D'Hondt *et al.* (2013), Yang *et al.* (2014), Liu *et al.* (2017), etc.

Lee *et al.* (2021) recently introduced another type of iterative bilateral filter, called gravitational filter, for speckle reduction in multi-look PolSAR data. As inspired by Newton's law of universal gravitation, a force of attraction

between two image pixels is formulated in polarimetric-spatial domain based on the following principle: directly connected like pixels attract more; distantly separated unlike pixels attract less. Thus, the attractive force is given by

$$f = k \frac{s(\mathbf{C}_1, \mathbf{C}_2)}{r^2}, \tag{3}$$

where k is a constant of proportionality. From (3), it is obvious that the attractive force is directly proportional to the polarimetric similarity $s(\mathbf{C}_1, \mathbf{C}_2)$ and inversely proportional to the Euclidean distance r between the two pixels.

The polarimetric similarity measure can be obtained by exploiting the eigenvalues of complex multivariate F matrix $\mathbf{C}_1 \mathbf{C}_2^{-1}$ or $\mathbf{C}_2 \mathbf{C}_1^{-1}$ in two different forms, namely, Roy's largest eigenvalue and Hotelling-Lawley trace. For the former, the corresponding similarity measure is given by

$$s(\mathbf{C}_1, \mathbf{C}_2) = R^{-2} \tag{4}$$

with

$$R = \max\{ \lambda_{\max}(\mathbf{C}_1 \mathbf{C}_2^{-1}), \lambda_{\max}(\mathbf{C}_2 \mathbf{C}_1^{-1}) \}, \tag{5}$$

where max denotes the maximum operator and $\lambda_{\max}$ refers to the largest eigenvalue. Alternatively, the similarity measure based on the latter is in form of

$$s(\mathbf{C}_1, \mathbf{C}_2) = T^{-2} \tag{6}$$

with

$$T = \max\{ q^{-1} \operatorname{tr}(\mathbf{C}_1 \mathbf{C}_2^{-1}), q^{-1} \operatorname{tr}(\mathbf{C}_2 \mathbf{C}_1^{-1}) \}. \tag{7}$$

The operator tr represents the matrix trace. Both the Roy's largest eigenvalue and the Hotelling-Lawley trace turn into the well-known intensity ratio (Touzi *et al*., 1988) when applying to intensity data (i.e., $q = 1$).

In the gravitational filter, the bilaterally filtered covariance matrix $\mathbf{C}_{\text{out}}$ is expressed as

$$\mathbf{C}_{\text{out}} = \left(f_o \mathbf{C}_o + \sum_{i=1}^{N-1} f_i \mathbf{C}_i \right) \Big/ \left(f_o + \sum_{i=1}^{N-1} f_i \right). \tag{8}$$

The matrix $\mathbf{C}_o$ is the covariance matrix of the currently processed pixel (or the central pixel in other words), while $\mathbf{C}_i$ refers to the covariance matrix of other pixels within the local window. The variable N denotes the total number of pixels within the test window. The filtering weight f_i is the attractive force as defined in (3) with $s(\mathbf{C}_o, \mathbf{C}_i)$, while f_o is given by

$$f_o = \max\{ f_1, f_2, \ldots, f_{N-1} \}. \tag{9}$$

The weighting increases with an increased similarity, but it is in a reverse way with respect to the spatial distance.

Since the gravitational filter is iterative, it can be written in time domain t as

$$\mathbf{C}_o^{t+\Delta t} = \mathbf{C}_o^t + \frac{\Delta t}{f_o^t + \sum_{i=1}^{N-1} f_i^t} \sum_{i=1}^{N-1} f_i^t (\mathbf{C}_i^t - \mathbf{C}_o^t), \tag{10}$$

where $\Delta t = 1$. The reader may compare (10) with the PolSAR anisotropic diffusion (Ma *et al*., 2015, p. 1043; Ma *et al*., 2018, p. 746). Notably, the anisotropic diffusion uses only a small and directly connected neighbourhood in its filtering.

In this study, the gravitational filter was applied for speckle reduction in the four-look ALOS-2 PALSAR-2 fully polarimetric data and benchmarked against two selected existing PolSAR filters, namely 1) refined Lee filter and 2) boxcar filter. Further analysis of the speckle filtering results is given in Section 4.

3.3 Geocoding and Mosaicking

As defined in Curlander and McDonough (1991, p. 371), geocoding is a geometric transformation process of an image data into map grid, while mosaicking refers to the process of assembling multiple independently geocoded images into a single frame. Prior to the mosaicking, the geodetic coordinates (i.e., longitude and latitude) of selected control points, which were provided based on the Geodetic Reference System 1980, were first converted into the Universal Transverse Mercator map coordinates (i.e., easting and northing). The ALOS-2 PALSAR-2 speckle-filtered polarimetric data were subsequently geocoded by using second-order polynomial equations:

$$X = a_0 + a_1 x + a_2 y + a_3 xy + a_4 x^2 + a_5 y^2 \tag{11}$$

and

$$Y = b_0 + b_1 x + b_2 y + b_3 xy + b_4 x^2 + b_5 y^2, \tag{12}$$

where the map coordinates x and y refer separately to the easting and northing. The image coordinates X and Y are the column and row numbers, respectively. Each polynomial equation contains six unknown coefficients. Since the number of the selected control points was more than the number of the unknown polynomial coefficients in this study,

least squares method was then employed to solve the overdetermined system for the latter.

After geocoding with nearest neighbour resampling method, a common pixel of the two partially overlapped ALOS-2 PALSAR-2 fully polarimetric images was chosen for determining the offsets in *X*- and *Y*-axis. The two geocoded images were then assembled through a straightforward shifting in both the axes. Figure 2 presents the ALOS-2 PALSAR-2 speckle-filtered polarimetric mosaic over Singapore, where the HH, HV, and VV intensities are displayed in the red, green, and blue (RGB) colour space. The filtering was conducted by using the two-iteration gravitational filter based on the Hotelling-Lawley trace with a 7×7 window. Note that only diagonal elements in the polarimetric covariance matrix were employed for computing the filtering weight in (3).
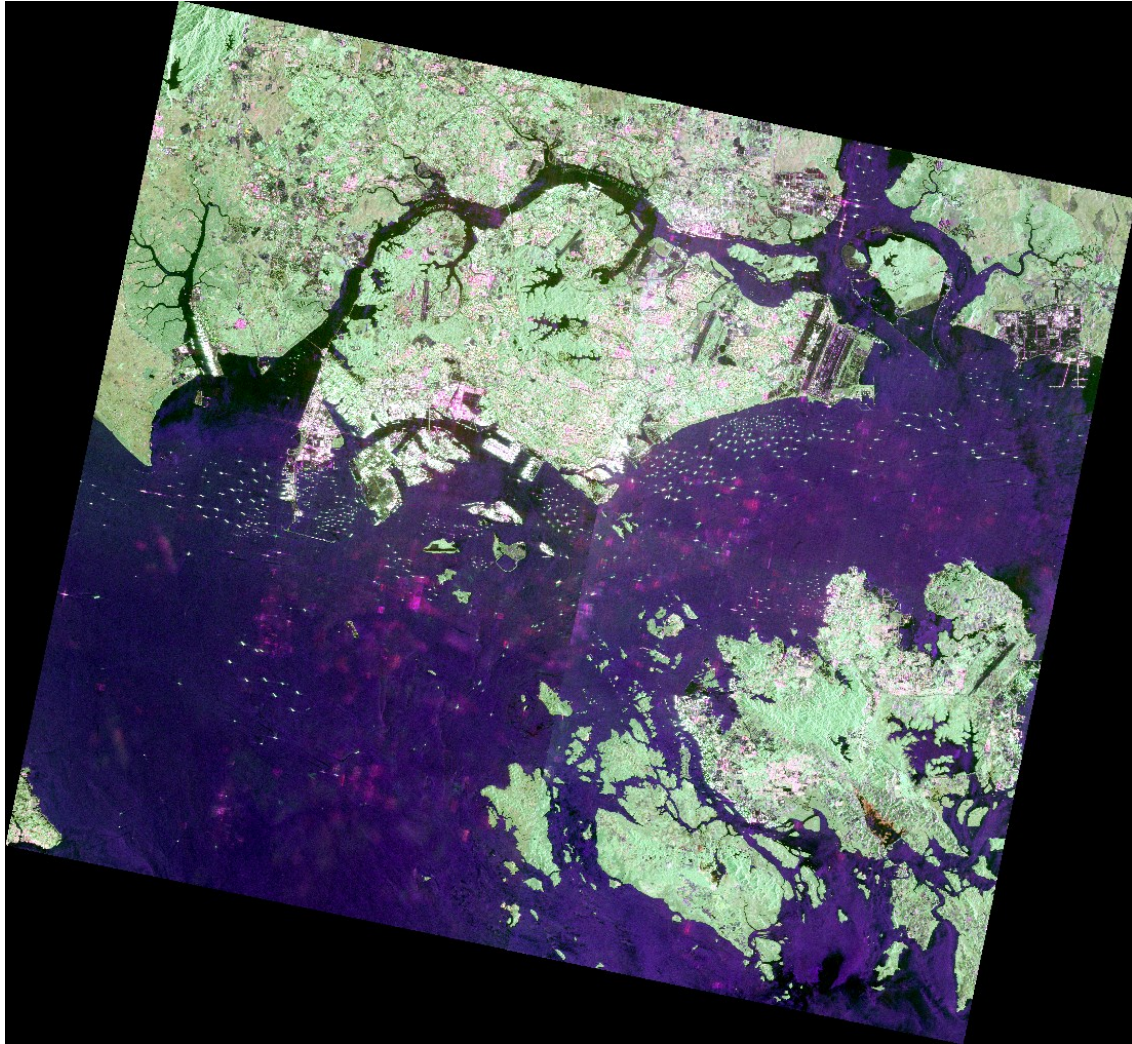

Figure 2: ALOS-2 PALSAR-2 speckle-filtered polarimetric mosaic.

3.4 Physical Scattering Decomposition

The retrieval of physical scattering properties of different land cover features from fully PolSAR data has long been studied. A three-component scattering model was developed by Freeman and Durden (1992, 1998) for multi-look PolSAR data. Their model involves physical fitting of a combination of double-bounce, surface, and volume scattering mechanisms. Yamaguchi *et al*. (2005) extended the Freeman-Durden model by adding helix scattering. One well-known problem associated with the model-based decomposition is the presence of negative scattering powers, which is inconsistent with the actual scattering phenomenon. To tackle this problem, many different solutions have been proposed and can be found in An *et al*. (2010), van Zyl *et al*. (2011), Lee *et al*. (2014), etc.

Lee *et al*. (2019) presented an iterative multistage polarimetric decomposition, which is inspired by the generalised odd-bounce and double-bounce scattering models (Chen *et al*., 2014), for reducing the negative power pixels. Together with the use of two roll-invariant volume scattering models, the iterative multistage decomposition combines both the three- and four-component decompositions. Its processing steps, which operate on a pixel-by-pixel basis, are shown in Figure 3. The reader is referred to Lee *et al*. (2019) for the mathematical details of the proposed iterative multistage decomposition. In this study, the iterative multistage decomposition was applied to the ALOS-2 PALSAR-2 polarimetric mosaic. The obtained decomposition results are discussed in Section 4.
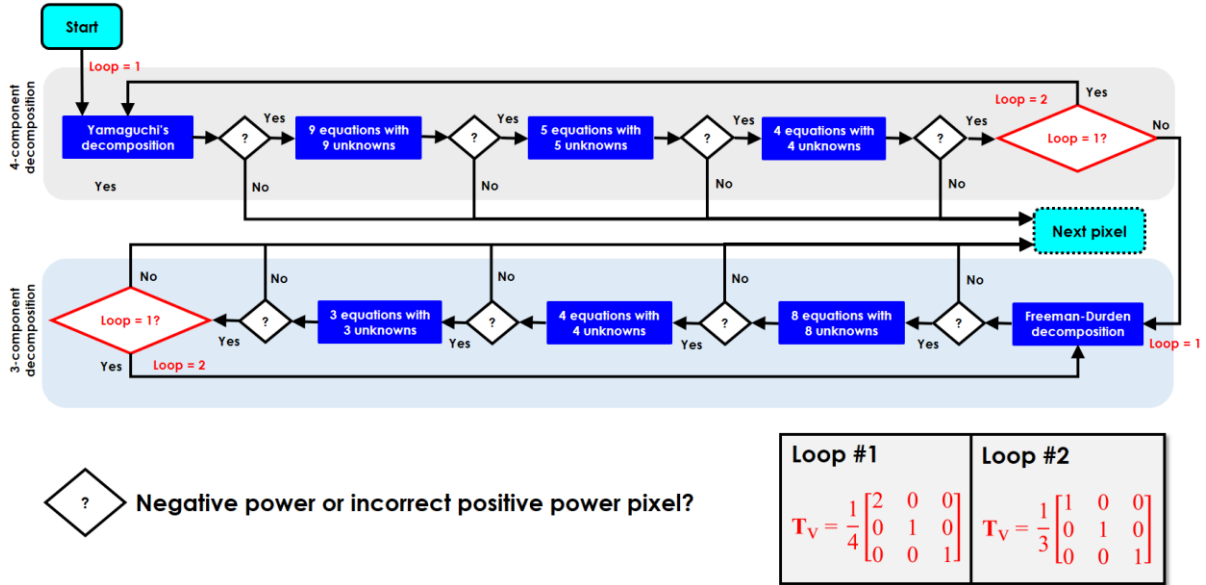
Figure 3: Iterative multistage polarimetric decomposition.

4. RESULTS AND DISCUSSION

4.1 Speckle Filtering

For speckle filtering in the four-look ALOS-2 PALSAR-2 fully polarimetric data, the gravitational filter was examined by using three different window sizes ranging from 5×5 to 9×9. Moreover, the refined Lee filter and the boxcar filter were selected for comparisons. Figure 4 presents the speckle filtering sub-scenes over Kim Kim River, Johor. Visually, both the refined Lee filter and the gravitational filter show their good capabilities in reducing speckle and retaining meaningful image features, such as edges, lines, point-like targets, etc. The boxcar filter with a larger window size (i.e., 7×7 window) smears out the image features expectedly.

Four essential aspects of the filtering performance were investigated: 1) speckle reduction, 2) image feature retention, 3) polarimetric property preservation, and 4) computational efficiency. In overall, the performances of the gravitational filter in the four aspects were consistent with the previous findings given in Lee *et al*. (2021). The gravitational filter performed well in the first two aspects, but at the expense of an increased computational load. Table 2 and Table 3 tabulate the averaged covariance matrix elements of two selected regions containing forest and oil palm trees, respectively. As pointed out previously in Lee *et al*. (2021), a radiometric bias was observed when the full covariance matrix was employed in the gravitational filtering. In both the tables, the biases can be noticed particularly for the HH and VV intensities (i.e., $\langle c_{11} \rangle$ and $\langle c_{33} \rangle$), where the differences are within 0.5 decibels. Based on the tabulated intensity values, the use of only diagonal matrix elements for computing the attractive force in (3) can, however, help in reducing the biases.

Table 2: Averaged covariance matrix of forest before and after filtering with a 7×7 window

	$\langle c_{11} \rangle$	$\langle c_{22} \rangle$	$\langle c_{33} \rangle$	$\langle \Re(c_{12}) \rangle$	$\langle \Im(c_{12}) \rangle$	$\langle \Re(c_{23}) \rangle$	$\langle \Im(c_{23}) \rangle$	$\langle \Re(c_{13}) \rangle$	$\langle \Im(c_{13}) \rangle$
Unfiltered	0.171	0.094	0.154	-0.001	0.001	-0.001	0.000	0.047	-0.002
Boxcar filter	0.171	0.094	0.154	-0.001	0.000	-0.001	0.000	0.047	-0.002
Refined Lee filter	0.169	0.093	0.152	-0.001	0.000	-0.001	0.000	0.046	-0.002
Gravitational filter with Roy's largest eigenvalue (number of iterations = 2)									
Full matrix	0.160	0.088	0.144	-0.001	0.000	-0.001	0.000	0.043	-0.002
Diagonal elements only	0.166	0.092	0.149	-0.001	0.000	-0.001	0.000	0.045	-0.002
Gravitational filter with Hotelling-Lawley trace (number of iterations = 2)									
Full matrix	0.161	0.088	0.144	-0.001	0.000	-0.001	0.000	0.044	-0.002
Diagonal elements only	0.166	0.092	0.149	-0.001	0.000	-0.001	0.000	0.045	-0.002

Note that $\Re(.)$ and $\Im(.)$ represent the real and imaginary parts, respectively.
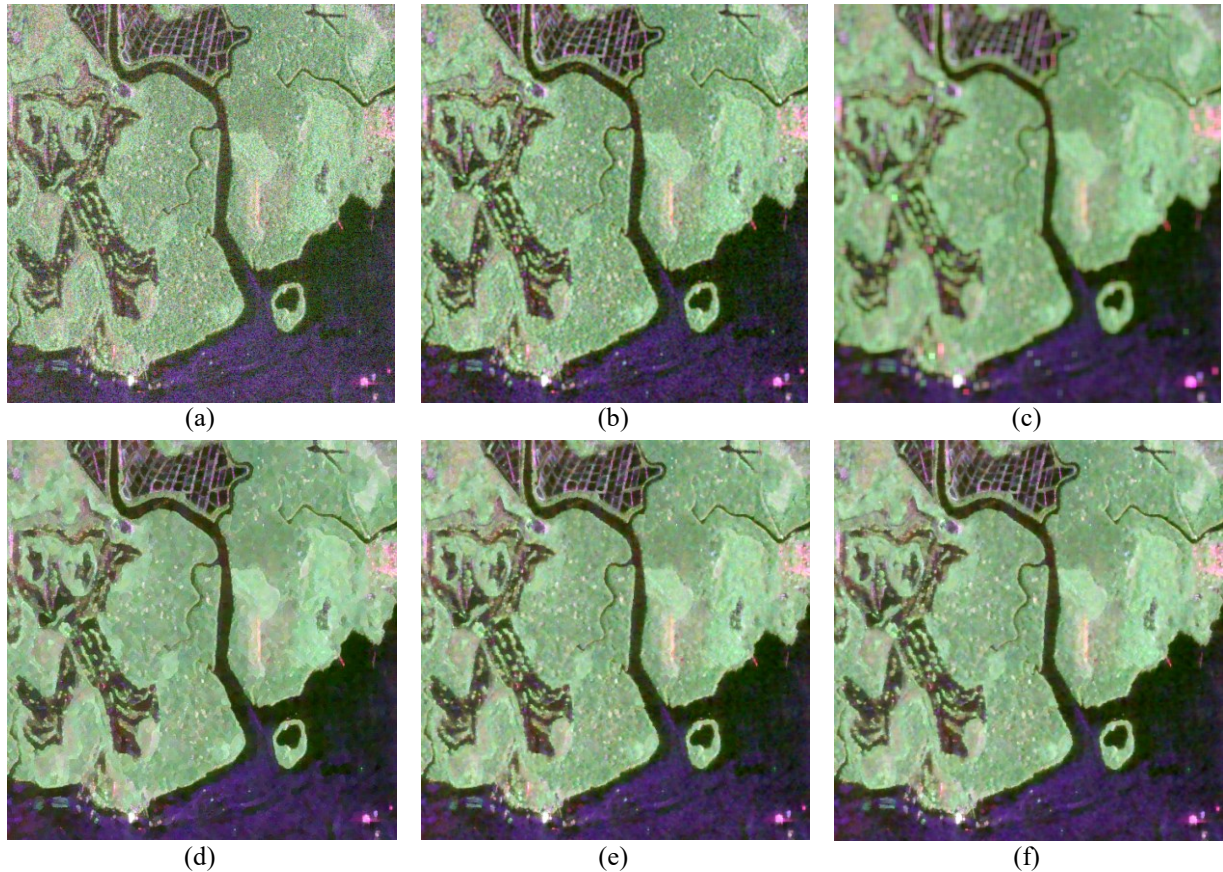
Figure 4: Speckle filtering results. (a) ALOS-2 PALSAR-2 unfiltered data with HH, HV, and VV intensities (in decibels) displayed in the RGB colour space. (b) Boxcar filter (3×3 window). (c) Boxcar filter (7×7 window). (d) Refined Lee filter (7×7 window). (e) Gravitational filter with Roy's largest eigenvalue (7×7 window, full matrix, $N_{itr} = 2$). (f) Gravitational filter with Hotelling-Lawley trace (7×7 window, full matrix, $N_{itr} = 2$). Note that N_{itr} refers to the number of iterations.

Table 3: Averaged covariance matrix of oil palm plantation before and after filtering with a 7×7 window

	$\langle c_{11} \rangle$	$\langle c_{22} \rangle$	$\langle c_{33} \rangle$	$\langle \Re(c_{12}) \rangle$	$\langle \Im(c_{12}) \rangle$	$\langle \Re(c_{23}) \rangle$	$\langle \Im(c_{23}) \rangle$	$\langle \Re(c_{13}) \rangle$	$\langle \Im(c_{13}) \rangle$
Unfiltered	0.223	0.044	0.136	0.000	0.000	0.000	0.000	0.060	-0.017
Boxcar filter	0.223	0.044	0.135	0.000	0.000	0.000	0.000	0.059	-0.017
Refined Lee filter	0.220	0.044	0.135	0.000	0.000	0.000	0.000	0.059	-0.017
Gravitational filter with Roy's largest eigenvalue (number of iterations = 2)									
Full matrix	0.210	0.042	0.128	0.000	0.000	0.000	0.000	0.056	-0.016
Diagonal elements only	0.217	0.043	0.132	0.000	0.000	0.000	0.000	0.058	-0.016
Gravitational filter with Hotelling-Lawley trace (number of iterations = 2)									
Full matrix	0.211	0.042	0.128	0.000	0.000	0.000	0.000	0.057	-0.016
Diagonal elements only	0.217	0.044	0.132	0.000	0.000	0.000	0.000	0.057	-0.016

4.2 Physical Scattering Decomposition

Prior to the polarimetric decomposition, the coherency matrix was obtained by linearly converting from the speckle-filtered covariance matrix (Cloude and Pottier, 1996, p. 501). An iterative multistage four-component decomposition, which was previously proposed by Lee *et al*. (2019), was then applied to the ALOS-2 PALSAR-2 speckle-filtered polarimetric mosaic. Figure 2 shows an extract of the polarimetric scattering decomposition result over Pulau Ubin in Singapore, where the double-bounce, volume, and odd-bounce scattering powers are displayed in the RGB colour space. Visually, the water surface shows predominantly the odd-bounce scattering, while the volume scattering is the dominant scattering component over the vegetated areas. The double-bounce scattering can be partially observed over Johor Port, which is located at the upper-left corner.

From the decomposition result, a large amount of negative power pixels over vegetated areas were significantly reduced by comparing with the Freeman-Durden three-component decomposition and Yamaguchi's four-component decomposition. The total number of the remaining negative power pixels was only 0.006% (i.e., 9114 pixels). The

majority of the remaining negative power pixels belonged to man-made objects. Table 4 lists the number of negative power pixels and incorrect positive power pixels resulting from different decomposition schemes. There were two different volume scattering models under study: 1) volume scattering model based on uniform distribution and 2) volume scattering model with total randomness. As can be seen in Table 4, the latter was found to reduce more negative power pixels than the former, which is similar to the previous finding in Lee *et al.* (2019).

In order to study the scattering mechanisms of different land cover types, each pixel is classified by identifying its dominant scattering contribution. Table 5 presents the percentage of different scattering components of selected land cover classes. All the vegetation classes (including the mangrove forest, secondary forest, oil palm, and shrub) showed their dominant volume scattering. The surface scattering was the main component for the bare land, water surface, and runway. The Malaysia-Singapore Second Link was dominated by the double-bounce scattering. In the built-up 1, the buildings were perpendicular to the radar illumination and exhibited the expected double-bounce scattering behaviour. On the contrary, the built-up 2 was composed of oriented buildings, which made nearly 45° from the direction of the radar illumination. The volume scattering was found to be dominant over the oriented buildings.
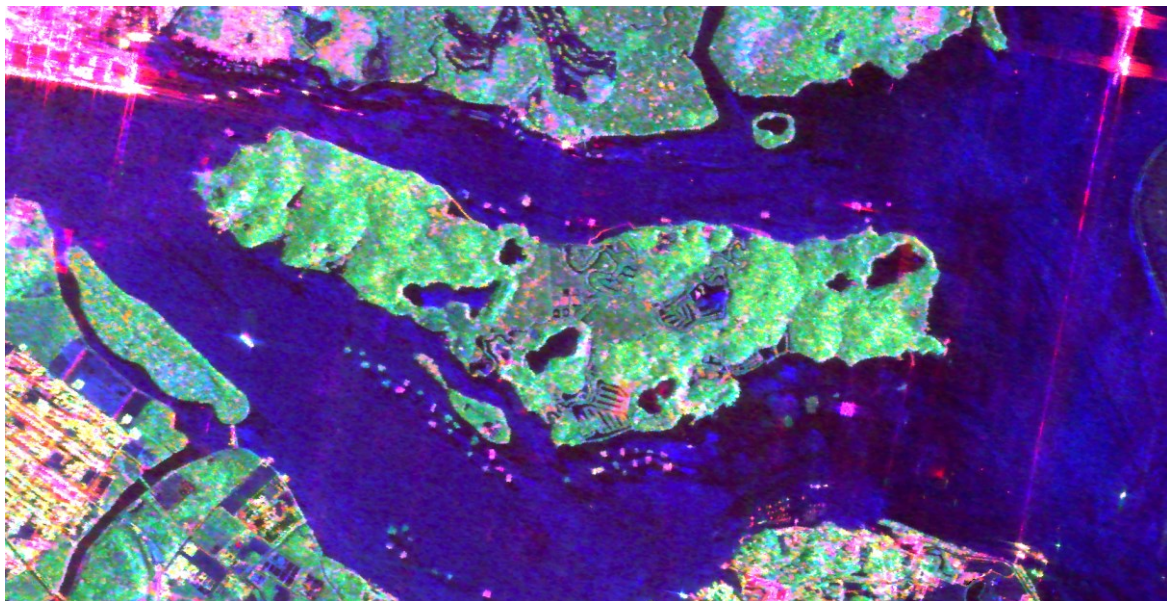

Figure 5: Physical scattering decomposition of ALOS-2 PALSAR-2 polarimetric mosaic.

Table 4: Number of negative power pixels and incorrect positive power pixels

	Negative power pixels	Incorrect positive power pixels
Volume scattering model based on uniform distribution		
Freeman-Durden three-component decomposition	17672384	2144628
Yamaguchi's four-component decomposition	14329039	1414473
Multistage four-component decomposition	3072396	-
Volume scattering model with total randomness		
Freeman-Durden three-component decomposition	6027919	-
Yamaguchi's four-component decomposition	6140369	7706
Multistage four-component decomposition	447254	-

Table 5: Scattering mechanisms (in percent) of different land cover types

	Number of pixels	Surface	Double-bounce	Volume	Helix	Unclassified
Bare land	5439	**100.00**	-	-	-	-
Bridge	1510	2.05	**87.88**	10.07	-	-
Built-up 1	8296	21.70	**78.22**	0.08	-	-
Built-up 2	6641	2.33	6.78	**90.86**	-	0.03
Mangrove forest	21228	0.16	0.09	**99.75**	-	-
Oil palm	12322	12.34	-	**87.66**	-	-
Runway	994	**91.65**	1.71	6.64	-	-
Secondary forest	29516	0.02	-	**99.98**	-	-
Shrub	6552	0.20	-	**99.80**	-	-
Water	80600	**100.00**	-	-	-	-

5. CONCLUSIONS

The speckle filtering and polarimetric scattering decomposition of the ALOS-2 PALSAR-2 fully polarimetric mosaic were carried out and reported in this paper. The processing steps involved 1) multi-looking, 2) speckle filtering, 3) geocoding, 4) mosaicking, and 5) model-based polarimetric decomposition. For the speckle filtering, the recently proposed gravitation-based bilateral filter was examined. Compared with the existing PolSAR bilateral filters, the gravitational filter is simple in concept and consists of less filtering parameters, which are needed to be tuned. Benchmarking against the refined Lee filter and the boxcar filter, the experimental results on the ALOS-2 PALSAR-2 polarimetric data confirmed the effectiveness of the gravitational filter in speckle reduction and image feature retention. For the polarimetric scattering decomposition, an iterative multistage four-component decomposition, which was previously introduced by Lee *et al*. (2019), was applied to the ALOS-2 PALSAR-2 speckle-filtered polarimetric mosaic. From the decomposition result, the negative power pixels over vegetated areas were largely reduced, where the total number of the remaining negative power pixels was only 0.006%.

ACKNOWLEDGMENT

REFERENCES

A. Alonso-González, C. López-Martínez, P. Salembier, and X. Deng (2013). Bilateral Distance Based Filtering for Polarimetric SAR Data. *Remote Sensing*, 5, pp. 5620−5641.

W. An, Y. Cui, and J. Yang (2010). Three-Component Model-Based Decomposition for Polarimetric SAR Data. *IEEE Transactions on Geoscience and Remote Sensing*, 48(6), pp. 2732–2739.

O. Antropov, Y. Rauste, A. Lönnqvist, and T. Häme (2012). PolSAR Mosaic Normalization for Improved Land-Cover Mapping. *IEEE Geoscience and Remote Sensing Letters*, 9(6), pp. 1074−1078.

V. Aurich and J. Weule (1995). Non-Linear Gaussian Filters Performing Edge Preserving Diffusion. *Proceedings of DAGM-Symposium*, pp. 538–545.

S.-W. Chen, X.-S. Wang, S.-P. Xiao, and M. Sato (2014). General Polarimetric Model-Based Decomposition for Coherency Matrix. *IEEE Transactions on Geoscience and Remote Sensing*, 52(3), pp. 1843–1855.

S. R. Cloude (2009). *Polarisation*: *Applications in Remote Sensing*. Oxford University Press, Oxford.

S. R. Cloude and E. Pottier (1996). A Review of Target Decomposition Theorems in Radar Polarimetry. *IEEE Transactions on Geoscience and Remote Sensing*, 34(2), pp. 498–518.

J. C. Curlander (1984). Utilization of Spaceborne SAR Data for Mapping. *IEEE Transactions on Geoscience and Remote Sensing*, GE-22(2), pp. 106−112.

J. C. Curlander, R. Kwok, and S. S. Pang (1987). A Post-Processing System for Automated Rectification and Registration of Spaceborne SAR Imagery. *International Journal of Remote Sensing*, 8(4), pp. 621−638.

J. C. Curlander and R. N. McDonough (1991). *Synthetic Aperture Radar*: *Systems and Signal Processing*. John Wiley, New York.

O. D'Hondt, S. Guillaso, and P. Hellwich (2013). Iterative Bilateral Filtering of Polarimetric SAR Data. *IEEE Journal of Selected Topics in Applied Earth Observations and Remote Sensing*, 6(3), pp. 1628−1639.

A. Freeman and S. Durden (1992). A Three-Component Scattering Model to Describe Polarimetric SAR Data. *SPIE Proceedings*, vol. 1748, pp. 213–224.

A. Freeman and S. L. Durden (1998). A Three-Component Scattering Model for Polarimetric SAR Data. *IEEE Transactions on Geoscience and Remote Sensing*, 36(3), pp. 963–973.

L. K. Kwoh, X. Huang, and M. Li (1997). Mosaiking of ERS SAR Quicklook Imagery of South East Asia. *Proceedings of the IEEE Geoscience and Remote Sensing Symposium*, pp. 249−251.

R. Kwok, J. C. Curlander, and S. S. Pang (1990). An Automated System for Mosaicking Spaceborne SAR Imagery. *International Journal of Remote Sensing*, 11(2), pp. 209−223.

J. S. Lee, T. L. Ainsworth, and Y. Wang (2014). Generalized Polarimetric Model-Based Decompositions Using Incoherent Scattering Models. *IEEE Transactions on Geoscience and Remote Sensing*, 52(5), pp. 2474−2491.

J.-S. Lee and E. Pottier (2009). *Polarimetric Radar Imaging*: *From Basics to Applications*. CRC Press, Boca Raton.

K. Y. Lee, C. G. Hou, S. C. Liew, and L. K. Kwoh (2019). Iterative Multistage Model-Based Decomposition for Polarimetric Synthetic Aperture Radar Imagery. *Proceedings of the 40ᵗʰ Asian Conference on Remote Sensing*, paper no. TuSS3-5.

K. Y. Lee, C. G. Hou, S. C. Liew, and L. K. Kwoh (2021). Gravitation-Based Bilateral Filtering of ALOS-2 PALSAR-2 Polarimetric Data. *Proceedings of the IEEE International Geoscience and Remote Sensing Symposium*, pp. 4747−4750.

L. Liu, F. Zhou, J. Chen, X. Yang, L. Jia, Z. Dong, and J. Ai (2017). Despeckling PolSAR Images with an Adaptive Bilateral Filter. *Journal of Applied Remote Sensing*, 11(2), p. 020501.

X. Ma, H. Shen, L. Zhang, J. Yang, and H. Zhang (2015). Adaptive Anisotropic Diffusion Method for Polarimetric SAR Speckle Filtering. *IEEE Journal of Selected Topics in Applied Earth Observations and Remote Sensing*, 8(3), pp. 1041−1050.

X. Ma, P. Wu, Y. Wu, and H. Shen (2018). A Review on Recent Developments in Fully Polarimetric SAR Image Despeckling. *IEEE Journal of Selected Topics in Applied Earth Observations and Remote Sensing*, 11(3), pp. 743−758.

G. Schreier, D. Kosmann, and A. Roth (1990). Design Aspects and Implementation of a System for Geocoding Satellite SAR-Images. *ISPRS Journal of Photogrammetry and Remote Sensing*, 45, pp. 1−16.

M. Shimada and O. Isoguchi (2002). JERS-1 SAR Mosaics of Southeast Asia Using Calibrated Path Images. *International Journal of Remote Sensing*, 23(7), pp. 1507−1526.

M. Shimada and T. Ohtaki (2010). Generating Large-Scale High-Quality SAR Mosaic Datasets: Application to PALSAR Data for Global Monitoring. *IEEE Journal of Selected Topics in Applied Earth Observations and Remote Sensing*, 3(4), pp. 637−656.

V. Syrris, C. Corbane, M. Pesaresi, and P. Soille (2020). Mosaicking Copernicus Sentinel-1 Data at Global Scale. *IEEE Transactions on Big Data*, 6(3), pp. 547−557.

C. Tomasi and R. Manduchi (1998). Bilateral Filtering for Gray and Color Images. *Proceedings of the IEEE International Conference on Computer Vision*, pp. 839−846.

R. Touzi, A. Lopes, and P. Bousquet (1988). A Statistical and Geometrical Edge Detector for SAR Images. *IEEE Transactions on Geoscience and Remote Sensing*, 26(6), pp. 764−773.

J. van Zyl and Y. Kim (2011). *Synthetic Aperture Radar Polarimetry*. John Wiley, New Jersey.

J. J. van Zyl, M. Arii, and Y. Kim (2011). Model-Based Decomposition of Polarimetric SAR Covariance Matrices Constrained for Nonnegative Eigenvalues. *IEEE Transactions on Geoscience and Remote Sensing*, 49(9), pp. 3452−3459.

Y. Yamaguchi (2020). *Polarimetric SAR Imaging*: *Theory and Applications*. CRC Press, Boca Raton.

Y. Yamaguchi, T. Moriyama, M. Ishido, and H. Yamada (2005). Four-Component Scattering Model for Polarimetric SAR Image Decomposition. *IEEE Transactions on Geoscience and Remote Sensing*, 43(8), pp. 1699−1706.

X. Yang, M. Ye, X. Wu, and Z. Yang (2014). Structure Preserving Bilateral Filtering for PolSAR Data. *Proceedings of the International Conference on Image Processing*, pp. 5846−5850.